An ESIPT-active α-naphtholphthalein-DAMN hydrazone as chromo-fluorogenic tweezers for fast detection of Al^{3+} ions

Daoyong Jiang[a,b,c], Tingfei Xie[d], Yizhao Chen[a,c], Xiuwen Zhang[c], Jihong Chen[d], Xiaowei Qi[e], Pengfei Zhang[c,*], Yong Wang[a,*]

[a]Postdoctoral Innovation Practice Base, Shenzhen Polytechnic University, Shenzhen 518055, China.

[b]Department of Chemistry and Pharmacy, Guilin Normal College, Guilin 541199, China.

[c]Guangdong Key Laboratory of Nanomedicine, CAS Key Laboratory of Health Informatics, Shenzhen Bioactive Materials Engineering Lab for Medicine, Institute of Biomedicine and Biotechnology, Shenzhen Institute of Advanced Technology, Chinese Academy of Sciences, Shenzhen 518055, China.

[d]Department of Nephrology, The People's Hospital of Baoan Shenzhen, The Second School of Clinical Medicine, Southern Medical University, Shenzhen 518101, China.

[e]Department of Breast and Thyroid Surgery, Southwest Hospital, Third Military Medical University (Army Medical University), Chongqing 400038, China.

† Electronic supplementary information (ESI) available.

*Corresponding authors:
Dr. Pengfei Zhang (pf.zhang@siat.ac.cn); Prof. Yong Wang (wangyong1@szpt.edu.cn).

Abstract

ESIPT-based fluorochromes are a type of promising materials for the detection of various chemical/biological species, especially the metal cations. Herein, we elaborately designed a prototypical ESIPT-active α-naphtholphthalein- derived "turn-on" fluorogenic tweezers **NPDM** for selectively detecting and visualizing Al^{3+} in biological and environmental samples. **NPDM** was found to specifically interact with Al^{3+} with dual emissions, good sensitivity (50 s), large Stokes shifts (140 nm/176 nm) and low detection limit (16.3 nM). Noteworthily, the sensing mechanism of **NPDM** towards Al^{3+} involves metal ion-coordination induced fluorescence enhancement (CHEF), ESIPT "turn-on" effect as well as restricted intramolecular rotation (RIR), which has been supported by Job's plot, HRMS, ^{1}H NMR titrations, as well as detailed DFT calculations. Interestingly, the **NPDM**-Al^{3+} ensemble can act as a secondary chromo-fluorogenic tweezers for monitoring F^- with a low detection limit down to 34.8 nM level. Thus, an advanced molecular memory device was constructed based on the fluorescence ''off-on-off" strategy and its excellent sensing properties. Moreover, a portable smartphone-aided intelligent platform was fabricated to realize the in-field, cost-effective, and faithful detection of Al^{3+} in real environmental water samples. Significantly, **NPDM** was successfully employed for imaging the intracellular Al^{3+} and F^- ions in Hela cells without interference from the oxidative stress and it is the first reported smart molecular tweezers capable of determining the Al^{3+} ions formed during

electroporation inside living cells. Furthermore, the strategy developed here is valuable to develop novel practically beneficial luminous molecules and provide intelligent luminescent detection platform for point-of-care sensing of health-related ions species in the prospect.

Keywords: ESIPT, α-naphtholphthalein-DAMN hydrazone, Chromo-fluorogenic tweezers, Al^{3+}, Cell imaging, Portable detection

1. Introduction

Environmentally and/or biologically important ions species, as the notable food contaminants and environmental pollutants, can not only destroy ecosystems but also be terribly harmful to human health.[1-5] Among them, as the most plentiful metal element in the earth's crust, aluminum is a non-essential trace elements, widely exist in our daily life and adversely affect human health, and is largely applied to industrial production, however, these industrial activities can lead to the overexposure of Al^{3+} to environment, followed by excessive Al^{3+} accumulation in the body and plant, can damage the brain, occurring hypomnesia, Alzheimer's disease, may also cause kidney and liver insufficiency, osteoporosis and other diseases, as well as the abnormal growth of plant.[6-10] On the other hand, it has been treated as food contaminants to be regulated, as the permissible limit of WHO guideline for Al^{3+} in drinking water is ~7.4 μM, thus it is of great momentousness to develop an simple and efficient way to sensing the contaminants Al^{3+} ions in food and environment. At present, the existing conventional tools such as inductively coupled plasma-optical emission spectrometer/-mass spectrometry (ICP-OES/-MS), atomic absorption spectroscopy (AAS), and electrochemical method have already been used for detecting metal ions.[11-15] However, the flies in the ointment are that these methods have the deficiencies of complex and professional operation (user-unfriendly), poor portability, as well as high cost.[16] Nowadays, smartphone-integrated optical detection platform has emerged as a promising method for semi-quantitative or quantitative, low-cost, convenient, real-time and precise *in-field* analysis of metal ions and other targets.[17-21] Compared with naked visualization detection, the smartphone-assisted RGB color analysis allows a higher accuracy and sensitivity mainly benefit from the breakthrough of self- limitation of vision.[22] The above inadequacies would be addressed due to the fact that such a new strategy incorporating smartphone with optical probes can be easily expanded as a hand-held contaminant detector without the need of expensive and bulky instruments in the foreseeable future. Thus, it is meaningful and urgently needed to develop a portable, visualized, point-of-care (POC), accurate and handy optical analysis platform for Al^{3+} and other analytes detection in further research, especially in resource-limited environments.

Fluorogenic probe presents the benefits of methodological simplicity, brief reaction time, high sensitivity, low LOD, cost-efficiency, accuracy, and capability of noninvasive fluorescence imaging in biological systems

as compared with the conventional sensing protocols for specific metal ions.[23-33] Thus far, there has been a striking progress in fluorogenic probes for the sensing of Al^{3+} and other metal ions based on various sensing mechanisms.[34,35] The response mechanisms utilized for fluorogenic probe design generally involve the following: AIE (aggregation-induced emission),[36-38] ESIPT (excited state intramolecular proton transfer),[39-42] PET (photoinduced electron transfer),[43,44] ICT (intramolecular charge transfer),[45,46] CHEF (chelation-enhanced fluorescence),[47,48] FRET (fluorescence resonance energy transfer),[49,50] CL (chemiluminescence),[51-53] TBET (through bond energy transfer),[54,55] and TICT (twisting intramolecular charge transfer),[56] etc. Amongst them, ESIPT-active fluorogenic probes have gained considerable attention because they offer promising superiorities, such as large Stoke shift, strong brightness, high sensitivity and outstanding photostability. The existing researches demonstrate that the intramolecular H-bonding between H acceptor (=N- and C=O) and H donor (-OH and NH_2) groups is ordinarily essential for the ESIPT molecules. The most commonly used ESIPT fluorogenic building blocks including the typical backbones of SSB (salicylaldehyde-based Schiff-base), flavones, benzophenones and HPQ (hydroxyphenylquinazolinone), and the analogues of HBT (2-(2'-hydroxyphenyl)benzothiazole), HBI (2-(2'-hydroxyphenyl)benzimidazole) and HBO (2-(2'-hydroxyphenyl)benzoxazole), and so on.[57] Generally, ESIPT is a distinctive four-level phototautomerization process (Enol-Enol*-Keto*-Keto). More specifically, in the S_0 state, the molecules typically existing as an E form with the intramolecular H-bond, i.e., O—H···N, O—H···O, and N—H···N.[58] Upon photoexcitation to the E* form, proton transfer takes place from H donor to H acceptor to generate the K* form with the change of intramolecular H-bond (O···H—N, O···H—O, and N···H—N). The K* form can decaying radiatively return to the K form and then a RPT (reverse proton transfer) occurs to produce the original E form. According to the energy barrier difference of ESIPT, single-emission from E* form or dual emission from E* form and K* form can be experimentally observed. Thanks to this extremely fast photochemical process, ESIPT molecules are featured by some particularly charming traits that make them valuable for fluorogenic probes, bioimaging agents and OLEDs, etc.[59-62] In recent years, SSB-derivated ESIPT fluorophores have been popularly used for designing the fluorogenic probes for ions (metal cations and anions), small molecules, biomolecules, and chemicals and others because of their easy access to synthesize and modify as well as the excellent photophysical properties.[63-69] For example, Luxami et al. proposed that the ‘‘turn-on’’ fluorogenic probe for Al^{3+} can be constructed by ESIPT and AIEE mechanisms.[70] Murugesapandian et al. synthesized an all-in-one type ESIPT-active multi-stimuli responsive fluorescence probe with AIE feature.[71] Intriguingly, a kind of novel keto-salicylaldehyde azines as building blocks of AIEgens were synthesized recently by Tang et al.[72] Yoon et al. and Zhou et al. designed the ESIPT and AIE fluorogenic probes for biothiols based on salicylaldazine dyes.[73,74] To date, numerous ESIPT-active Schiff-base fluorogenic probes were developed for Al^{3+} detection.[75-90] Nevertheless, among them, only a few can

consistently maintain the ESIPT feature, and the design strategies are still very scarce.[91-94] Therefore, it is still urgently demanded novel fluorogenic probes with continuous ESIPT characteristic for Al^{3+} ions and other targets estimation overcoming these limitations.

In the light of the previous reports diaminomaleonitrile (DAMN)-based Schiff-base fluorogenic probes are fascinating due to their unique multiple reactive sites, especially the seductive binding features.[95-104] Recently, *Zheng Li et al.* have developed a DAMN-based dual channel emissive fluorogenic probe for the selective detection of Al^{3+}.[105] Additionally, this group have again reported a dual-response fluorogenic probe for Al^{3+} and Zn^{2+} based on a DAMN-benzothiazole hybrid.[106] Subsequently, *Yun Wang* and co-workers have constructed a new DAMN-based colorimetric and ratiometric fluorescence probe for highly selective monitor of $Al^{3+}$and ClO^{-}.[107] Unfortunately, so far only few DAMN-derived Schiff-base fluorogenic tweezers with continuous ESIPT property for Al^{3+} sensing that have been reported.[91,92] Hence the development of available ESIPT-active DAMN-derived fluorogenic tweezers for Al^{3+}, especially in biological systems, is still in its infancy. As well known, the imino-based molecules has weak fluorescence in either room temperature (RT) solution or solid state, which is ascribed to easier intramolecular motions via the double-bond torsion-causing photoinduced nonadiabatic decay (PIND) effect.[108] Such PIND-guided ESIPT molecules possess the remarkable potential to act as the advanced versatile fluorogenic probes. Inspired by this notion and to address the above concerns, in this work, the bistructure molecular tweezers **NPDM** with ESIPT property was developed successfully by using an α-naphtholphthalein-donor and dual DAMN acceptors bridged by two iminodouble bonds. Indeed, **NPDM** can specifically sensing Al^{3+} over other miscellaneous metal ions with significant "turn-on" dual emissions fluorescence features in aqueous DMSO mixture (Scheme 1). Impressively, apart from the HRMS and ^{1}H NMR methods, (TD)DFT calculations were also performed to further corroborate the binding mode and elucidate the Al^{3+}/F^{-}-switched ESIPT process theoretically and clarify the experimental results. By utilizing the two chemical inputs (Al^{3+}/F^{-}) and dual emission outputs, a molecular memory device was established. More intriguingly, the portable, semiquantitative, precise, visualized, and on-site sensing of Al^{3+} ions in water samples was achieved by a smartphone-based intelligent detection platform. What's more, **NPDM** was successfully employed for sensing the various concentrations of Al^{3+} and F^{-} in live HeLa cells with desirable biocompatibility and without interference from the intracellular oxidative stress. This study would lay the foundation for ESIPT-active fluorogenic tweezers with multiple functions in practical applications.

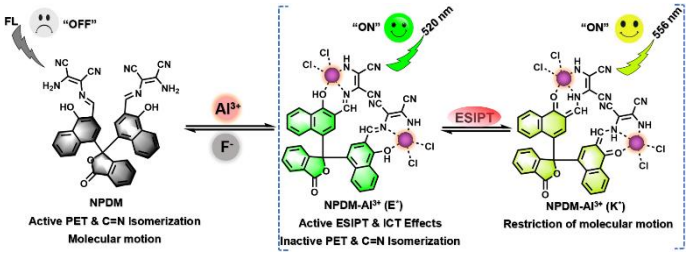

Scheme 1. Schematic illustration of the ESIPT-active regenerable fluoro-chromogenic molecular tweezers **NPDM** was employed for Al^{3+} and F^- assays.

2. Results and discussion

2.1 Synthesis

The fluorogenic tweezers **NPDM** was designed and easily obtained in two steps (Scheme S1). The intermediate NS was synthesized by the Duff reaction according to the previous work;[109] after that the **NPDM** was successfully synthesized via the Schiff-base condensation reaction between the NS and DAMN, which was also characterized using ^{1}H NMR, ^{13}C NMR, and HRMS (high-resolution mass spectrometry) (Fig. S1-S5, ESI).

2.2 Theoretical studies on the ESIPT effect of NPDM

We applied (TD)DFT calculations for systematical comprehension of the ESIPT effect in **NPDM** (Fig. 1). The molecular electrostatic potential (MEP) reveals the dispersions of electron density on the molecular surface, is an extremely useful tool for understanding of the H-bonding interaction.[110] So first, the electrostatic potential (ESP) surface of **NPDM** was calculated to disclose the activity of the hydrogen bond O−H···N. As shown in Fig. 1A, the electrostatic potentials of DAMN moieties were smaller than that of naphthols, indicating the accumulation of negative charges on the DAMN sites. Besides, the positive potentials of OH groups (H-bond donors) and the negative potentials of N atoms of the -C=N groups (H-bond acceptors) proving the existence of hydrogen bonds in **NPDM**. Additionally, the frontier molecular orbitals (FMOs) analysis was presented to further certify the existence of the ESIPT phenomenon. Although the electronic distributions over the ESIPT-generated K* form were closely resemble those of E* form, but the transformation from E* to K* form caused a lower energy gap between the HOMO and LUMO by 0.0781 eV (Fig. 1B). Thus, the diminished energy gap was precisely corresponding to the red-shift of emission maximum for K* form of **NPDM**. In addition, the IR vibrational spectra were simulated to analyse the variations of H-bonds strength of O-H groups (Fig. 1C). The comparative observation specified that the IR vibration frequency of O-H in the S_1 state showed a significant red shift of 326 cm^{-1} (from 3188 cm^{-1} to 2862 cm^{-1}), endorsing the the change in the geometric parameter of intramolecular H-bondings and enhancement phenomenon of H-bonds in the S_1 state, and implying the happening of ESIPT effect is more favorable.[111] Furthermore, in order to explore the inherent mechanism of the ESIPT effect, the 2D potential energy curves (PECs) of **NPDM** at the S_0(E) and S_1(E*) states were scanned separately according to the optimized structures (Fig. 1D). The

obtained PECs of **NPDM** are as the functions of O-H distance ranging from 0.9972 Å(initial length) to 2.3572 Å and 1.0072 Å(initial length) to 2.2872 Å at its S_0 and S_1 states respectively. As plotted in Fig. 1D, the forward energy barrier of 3.15 kcal/mol is higher than the reverse energy barrier (0.18 kcal/mol), manifesting that it is of difficulty to occur the proton transfer reaction at the S_0 state.[112] By contrast, there is almost no energy barrier in the S_1 state proton transfer. Hence, this is more favorable for the ESIPT process to proceed.

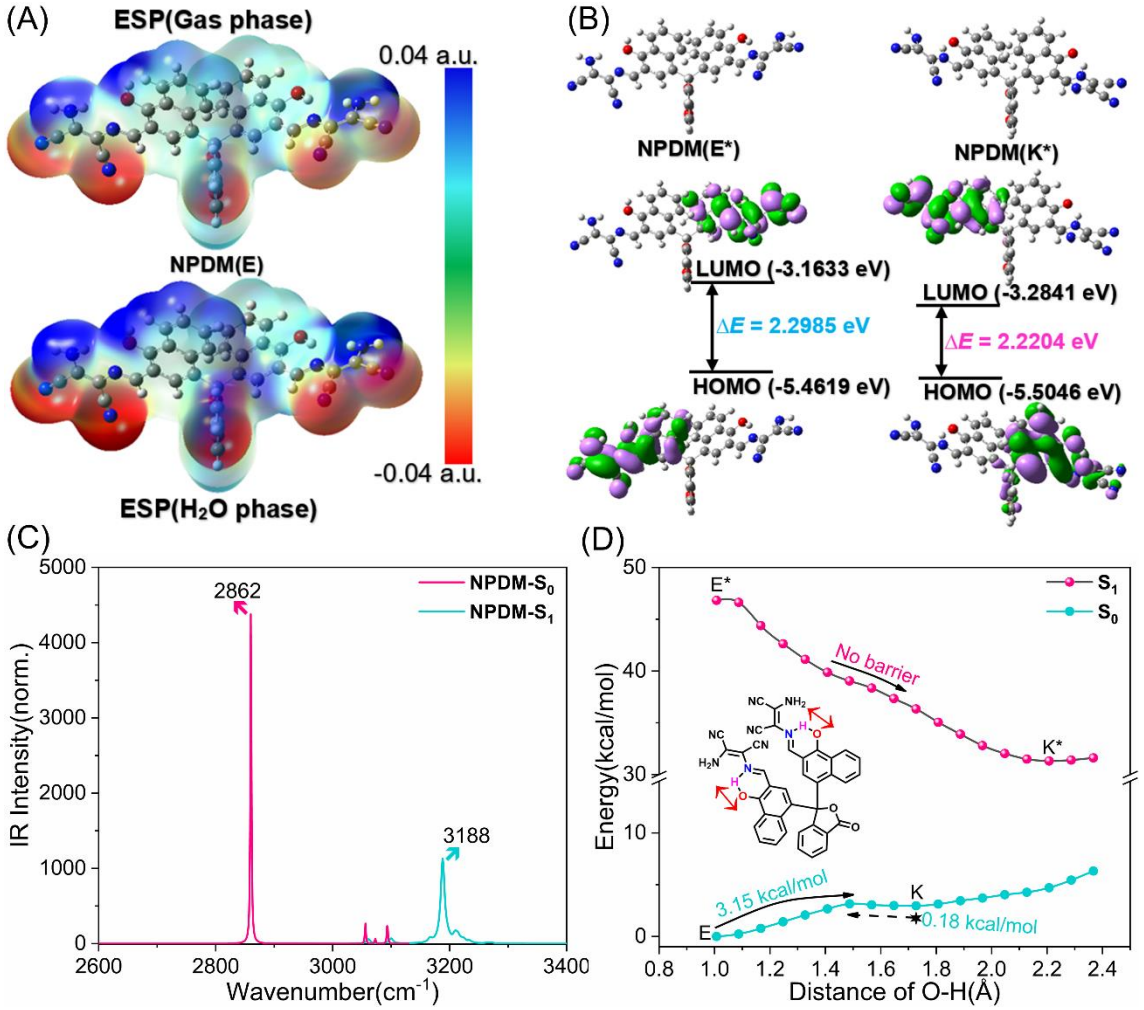

Fig. 1. (A) Electrostatic potential (ESP) map for **NPDM** in S_0 state (gas phase and H_2O phase)(Here, blue surface represents positive regions, while the red denotes the negative charge region on the ESP surface). (B) The calculated frontier molecular orbitals (HOMOs and LUMOs) of **NPDM** as well as corresponding energy level of the enol and keto form in the S_1 state. (C) Infrared vibration spectra of the O-H bond on the ground state S_0 and excited state S_1. (D) Potential energy curves in the S_0 and S_1 states for **NPDM** as a function of the O-H bond length. All data obtain based on the TD-DFT using B3LYP/6-31G(d)/6-311G(d) level.

2.3 The optical properties of NPDM for reversible detection of Al^{3+}

Primarily, colorimetric properties of **NPDM** towards Al^{3+} ions were investigated in aqueous DMSO solution (Fig. S6, ESI). The characteristic short-wavelength absorption bands (329 nm, 357 nm), and the longer absorption bands (414 nm, 473 nm and 502 nm) in UV-Vis spectrum of **NPDM** (10 μM) were due to π → π* transitions and charge transfers (CT) from the electron donors ((D, phenolic hydroxyl) to the acceptors (A, cyanogen) groups respectively.[113-115] Upon addition of Al^{3+} ions (20 μM), significant variations of absorption pattern were marked. The typical absorption band at 414 nm was bathochromic-shifted to 436 nm, and the

absorption maximum near 473 nm and 502 nm were enhanced along with a color change from yellowish brown to chrome yellow, which indicated that **NPDM** could coordinate with Al^{3+} ions. The above observations illustrated that **NPDM** can undergo a chromogenic response to Al^{3+} ions. In addition, the intrinsic optical properties of **NPDM** are very important. So, its emission spectrum was tested under the excitation of 380 nm in DMSO, and the emission maximum is observed around 547 nm (Fig. S7, ESI). The dual emissions could be attributed to ESIPT behavior of molecular tweezers **NPDM**.

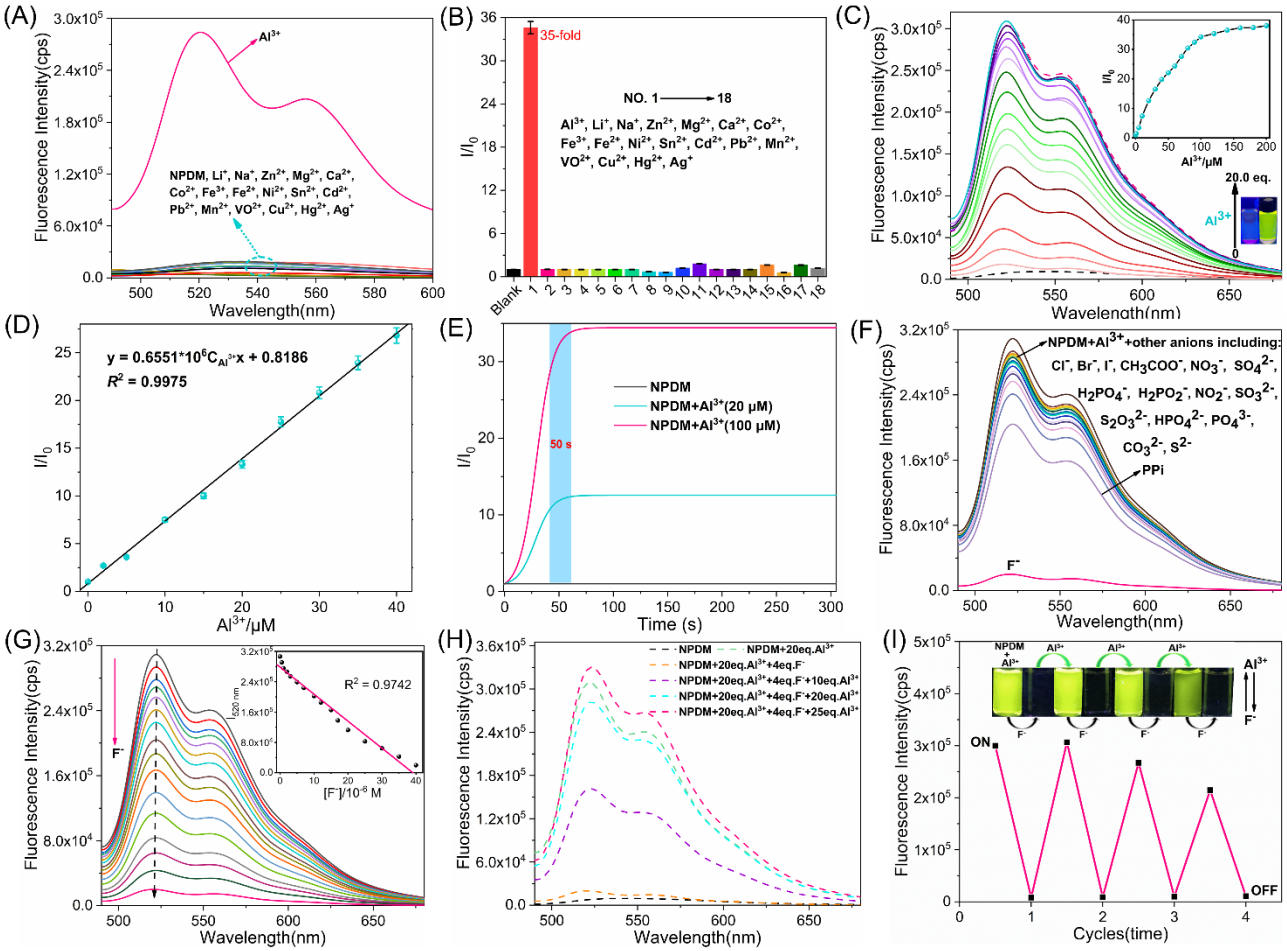

Fig. 2. (A) Fluorescence spectra of **NPDM** (10 μM) with Al^{3+} (100 μM) and various interference metal ions (200 μM) (Li^+, Na^+, Ag^+, Zn^{2+}, Mg^{2+}, Ca^{2+}, Co^{2+}, Fe^{3+}, Fe^{2+}, Ni^{2+}, Sn^{2+}, Cd^{2+}, Pb^{2+}, Mn^{2+}, VO^{2+}, Cu^{2+}, Hg^{2+}) in DMSO/H_2O (7/3, *v/v*, 10 mM, HEPES, pH 7.0) solution. (B) Relative fluorescence intensity variation of **NPDM** in the presence of various metallic ions at pH = 7.0. (C) Fluorescence titration spectra of **NPDM** (10 μM) with the increasing concentrations of Al^{3+} (0~200 μM) in DMSO/H_2O (7/3, *v/v*, 10 mM, HEPES, pH 7.0) solution (Insets: the relationship curve between the relative emission intensity of **NPDM** and concentrations of Al^{3+} at 520 nm/556 nm; fluorescence color change of **NPDM** without and with Al^{3+} under 365 nm UV light). (D) Linear relationship between emission intensity ratios and [Al^{3+}] (0~40 μM). (E) Time-fluorescence intensity of **NPDM** (10 μM) in the presence of Al^{3+} (20 μM and 100 μM) at 520 nm/556 nm in DMSO/H_2O (7/3, *v/v*, 10 mM, HEPES, pH 7.0) respectively. (F) Fluorescence spectra of the [**NPDM**-Al^{3+}] whole (10 μM in DMSO/H_2O (7/3, *v/v*, 10 mM, HEPES, pH 7.0)) was added with various external anions (100 μM) including Cl^-, Br^-, I^-, AcO^-, CO_3^{2-}, NO_3^-, NO_2^-, $S_2O_3^{2-}$, S^{2-}, SO_4^{2-}, SO_3^{2-}, $H_2PO_4^-$, $H_2PO_2^-$, HPO_4^{2-}, PO_4^{3-}, PPi and F^- (40 μM). (G) Fluorescence spectra: upon addition of [F^-] = 0, 0.5, 1,... 20, 25, 30, 35, 40, μM to DMSO/H_2O (7/3, *v/v*, 10 mM, HEPES, pH 7.0) mixture. (H) Emission spectra of **NPDM** (10 μM) by alternated adding Al^{3+} and F^- in DMSO-HEPES mixture. (I) Fluorescence intensity of **NPDM** (10 μM) at 520 nm & 556 nm upon alternate addition of a constant amount of Al^{3+} and F^-. Inset: photographs of fluorescence reversibility of **NPDM** - Al^{3+} and **NPDM** - Al^{3+} plus F^- in the mixture solution. (λ_{ex} = 380 nm; slits: 5/5 nm).

Then, we tested the fluorogenic responses of **NPDM** in the presence of Al^{3+} (100 μM) and other competitive

metallic ions (i.e, Li^{+}, Na^{+}, Ag^{+}, Zn^{2+}, Mg^{2+}, Ca^{2+}, Co^{2+}, Fe^{3+}, Fe^{2+}, Ni^{2+}, Sn^{2+}, Cd^{2+}, Pb^{2+}, Mn^{2+}, VO^{2+}, Cu^{2+}, Hg^{2+}, 200 μM) in DMSO/H_2O (7/3, *v/v*, 10 mM, HEPES, pH 7.0). As shown in Fig. 2A, **NPDM** alone has the faint fluorescence owing to C=N isomerizations and PET behaviors as well as the existence of strong electron withdrawing groups (-C≡N) in **NPDM**.[116,117] By contrast, as Al^{3+} was added to **NPDM** solution, a significant dual emission bands at 520 nm and 556 nm were observed, which may be the results of ESIPT processes, whereas there were no remarkable fluorescence variations of **NPDM** when other miscellaneous cations were introduced into **NPDM** solution respectively. The relative fluorescence intensity increased by 35 folds as compared with that of free **NPDM** (Fig. 2B). Further, the tolerance experiments were explored in the presence of competitive cations (Fig. S8, ESI). It showed that only Cu^{2+} obviously reduced the maximum emission intensities, however, this interference can be cleared up with the masking reagent dimethylglyoxime (DMG) for the distinction between Al^{3+} and other metallic ions.[118] These results implied that **NPDM** is highly selective to Al^{3+}. Furthermore, the fluorescence titration experiments were employed for investigating the interaction properties of **NPDM** towards Al^{3+}. As shown in Fig. 2C, fluorescence intensities of **NPDM** solution at 520 nm and 556 nm showed the linear growth up to 100 μM Al^{3+} and reached the equilibrium (200 μM) following the visual fluorescence change from colorless to strong green-yellow under a 365 nm UV lamp (Fig. 2C inset). The fluorescence enhancement of **NPDM** treated with Al^{3+} could be atrributed to the CHEF and ICT processes.[119] **NPDM**-Al^{3+} (Φ = 0.3404) complex implied about 37 folds higher Φ value than that of **NPDM** solution (Φ = 0.0096) at 520 nm. It's noteworthy that the appearance of remarkable dual emission bands at 520 nm and 556 nm with the introduction of Al^{3+} are contributed to coexistence of the forms (enol and keto) in phenolic Schiff base moieties and may be due to the excited tautomer of E* and K* forms arising because of ESIPT processes (Scheme 1). The emission bands at 520 nm and 556 belong to **NPDM**-Al^{3+} enol form and **NPDM**-Al^{3+} keto form respectively. Actually, if the chealation of **NPDM** with Al^{3+} trigger deprotonations of the phenolic hydroxyl groups (-OH), the ESIPT processes would not happen and **NPDM**-Al^{3+} complex only could emit a single emission band.[39,57] However, the deprotonation behaviours could not be observed, and thus ESIPT is not blocked and the dual emissions arising, which was also further supported by HRMS, ^{1}H NMR, and DFT studies. By plotting the relative emission intensities (I/I_0) at 520 nm versus the [Al^{3+}] (Fig. 2D), and according to the DL equation (3δ/slope), the LOD of **NPDM** for Al^{3+} was found as 16.3 nM (0-40 μM, R^2 = 0.9975), which is sufficiently below the maximum allowable level of Al^{3+} in potable water from the EPA (7.4 μM), revealing desirable sensitivity of **NPDM** for Al^{3+} ions. The stoichiometric ratio of **NPDM** chelated with Al^{3+} was obtained as 1:2 using Job's plot (Fig. S9, ESI). Depending on fluorescence titration data, the association constant between the **NPDM** and Al^{3+} was estimated to be 1.07 × 10^{10} M^{-2} by the Benesi-Hildebrand plot (Fig. S10, ESI), which displayed the binding affinity of **NPDM** to Al^{3+} was enough strong.

In addition, the time-dependent fluorescence response of tweezers **NPDM** (10 μM) for Al^{3+} was conducted in DMSO/H_2O (7/3, *v/v*, 10 mM, HEPES, pH 7.0) solution. As shown in Fig. 2E, after the introduction of Al^{3+} (20 μM, 100 μM) to **NPDM** solution respectively, the relative fluorescence intensity (at 520 nm) of **NPDM** quickly reached the equilibrium within 1min. Thus, the above results clearly proved that **NPDM** has great potential for the quick and real-time monitoring of Al^{3+}. To evaluate the practical application potential of **NPDM** in live organisms, the pH effect on the **NPDM** response to Al^{3+} was examined subsequently over the pH range of 4 to 11. (Fig. S11, ESI). In case of **NPDM** alone fluorescence intensity alterations are negligible at pH 4-11, whereas the **NPDM**-Al^{3+} complex exhibited noticeable fluorescence enhancement, especially at pH 6-8, suggesting the practical application potential for sensing Al^{3+} under physiological conditions. Finally, comparing with the recently reported Schiff-base-based fluorogenic probes for selectively sensing Al^{3+} which have similar conformations, **NPDM** manifests the superiorities in desirable sensitivity, satisfactory LOD, large Stokes shifts, rapid response, interaction mechanism, and broad preliminary applicable potentials (Table S1, ESI).

Repeatability is one of the crucial standard for most molecular probes and it is considered generally as the competence of the fluorescence probes designed to display uniform performances and give comparable sensitivity attributes when the molecular probes or mode are repeatedly used.[120] Thus, to qualitatively investigate the reversible sensing process of Al^{3+} by **NPDM**, we add no less than seventeen sorts of physiological and environmental-related anions: F^-, Cl^-, Br^-, I^-, AcO^-, $S_2O_3^{2-}$, NO_3^-, NO_2^-, CO_3^{2-}, S^{2-}, SO_4^{2-}, SO_3^{2-}, $H_2PO_4^-$, $H_2PO_2^-$, HPO_4^{2-}, PO_4^{3-}, and $P_2O_7^{4-}$ (PPi) into **NPDM**-Al^{3+} system (DMSO/H_2O, 7/3, v/v, 10 mM, HEPES, pH 7.0), respectively. As shown in Fig. 2F, upon interaction with interfering anions **NPDM**-Al^{3+} adduct showed negligible changes in fluorescence intensity, except that F^- (40 μM) caused reliable fluorescence quenching. Additionally, the fluorescence "ON-OFF" switching feature of **NPDM**-Al^{3+} ensemble is further verified by fluorescence titration experiments (Fig. 2G). With the progressive addition of F^- (0-40 μM), the emission intensities of **NPDM**-Al^{3+} at 520 nm & 556 nm were gradually declined and reached saturation state when 4 equiv. of F^- was added and up to 95% emission intensity of the complex system was quenched. The LOD for F^- was estimated to be 34.8 nM, which is not only superior to some previous secondary molecular tweezers for detecting F^-, but also well below the recommended dosage (79 μM) by WHO for potable water. Thus, the results suggested that fluorescence tweezers **NPDM** was reinstated during the sensing procedure of F^-. Moreover, to further corroborate the stability and reproducibility of the **NPDM**-Al^{3+} complex, we conduct F^--addition experiments. As shown in Fig. 2H, the periodically alternating introduction of given amount of Al^{3+} and F^- to the solution of **NPDM** led to a switchable alteration in the fluorescence spectrum. Interestingly enough, such 'off-on-off' fluorescence switching cycles could be repeated at least four times without compromising its sensitivity by modulating the addition of Al^{3+}/F^- (Fig.

2I) and this phenomenon manifests that **NPDM** alone has no direct response to the anions. Therefore, F^- anions binded to Al^{3+} ions through decomplexating Al^{3+} from the **NPDM**-Al^{3+} whole. Thus, assisted by F^- anions, the repeatability in case of Al^{3+} ions could be achieved. Nevertheless, these negative changes could be countervailable when the Al^{3+} concentration is in excess along with the corresponding fluorescence color variations under a UV-lamp (Fig. 2I inset). All the experimental data demonstrated that **NPDM** is an recyclable "off-on-off" molecular tweezers for Al^{3+} and F^-.

2.4 Proposed Mechanism

To better expound the sensing mechanism, HRMS, ^{1}H NMR and DFT calculations were studied. Upon addition of 1.0 equivalent of Al^{3+} into **NPDM**, the newly found unique ion peak at m/z = 749.08154 corresponding to [[**NPDM** + Al^{3+}] + 2Cl - H]$^-$ (calcd. [[**NPDM** + Al^{3+}] + 2Cl], m/z: 750.08780) (Fig. S12, ESI), which indicated that **NPDM** chelated with Al^{3+} to form the **NPDM**-Al^{3+} complex with 1:1 stoichiometry. Similarly, when the 2.0 equivalent of Al^{3+} was introduced into the solution, the existing molecular ion peak at m/z = 654.1764 (bare **NPDM**) disappeared to be replaced by a new ion peak at m/z = 776.10046 (negative mode) (Fig. S13, ESI), which can be assigned to [[**NPDM** + 2Al^{3+}] + 4H_2O - 2H]$^-$ (calcd. [[**NPDM** + 2Al^{3+}] + 4H_2O], m/z: 778.16609), further confirming the generation of **NPDM**-Al^{3+} whole with 1:2 stoichiometry, which is consisted with the Job's plot analysis. What's more, the ^{1}H NMR titration was also recorded in DMSO-d_6 to better understand the detailed interaction of **NPDM** with Al^{3+}. As provided in Fig. S14, with the addition of 2.0 equivalent of Al^{3+}, the proton H (phenolic-OH) at δ 12.26 ppm downfield shifted to 12.48 whereas the proton H (free -NH_2) at δ 7.40 ppm disappeared, meanwhile, a new peak (-NH) was formed at δ 9.38 ppm, which is caused by interaction between -NH_2 and Al^{3+}. In addition, the imine proton (8.57 ppm, HC=N) slightly upfield shifted to δ 8.51 ppm. Thus, the protonation state of the PhOH enables the ESIPT process remain unchanged in **NPDM**-Al^{3+} adduct. The above findings supported that the proposed mechanism of **NPDM** for Al^{3+} can be illustrated in Scheme 1.

It is envisaged that the dynamic intramolecular motions and relevant vibronic coupling in RT solution could hamper ESIPT.[121] Therefore, to decipher the fluorescence mechanism in RT solution, the PESs of the rotational C=N bond/C=C bond in the enol and keto form respectively in the S_1 states were firstly calculated by scanning the torsion angle (0° →180°) at 10° intervals (Fig. 3A-B). Theoretically, the conical intersection (CI) is one of nonradiative pathways and is detrimental to strong light emission with high quantum yield. In addition, the dwindling energy gaps between S_1 and S_0//S_1 (the vertical projected S_0 state) can cause an elevated rate of IC (internal conversion) and ultrafast nonradiative decay in terms of the energy-gap law.[122] As described by the excitation state double-bond rotations-guided PESs (potential energy surfaces), twisting around the imino/vinyl-double bond can yield the CI at the 90° torsional angle. These imply that the excited **NPDM** molecule can be efficiently inactivated to S_0//S_1 state via the CI pathway of nonradiative IC, after that

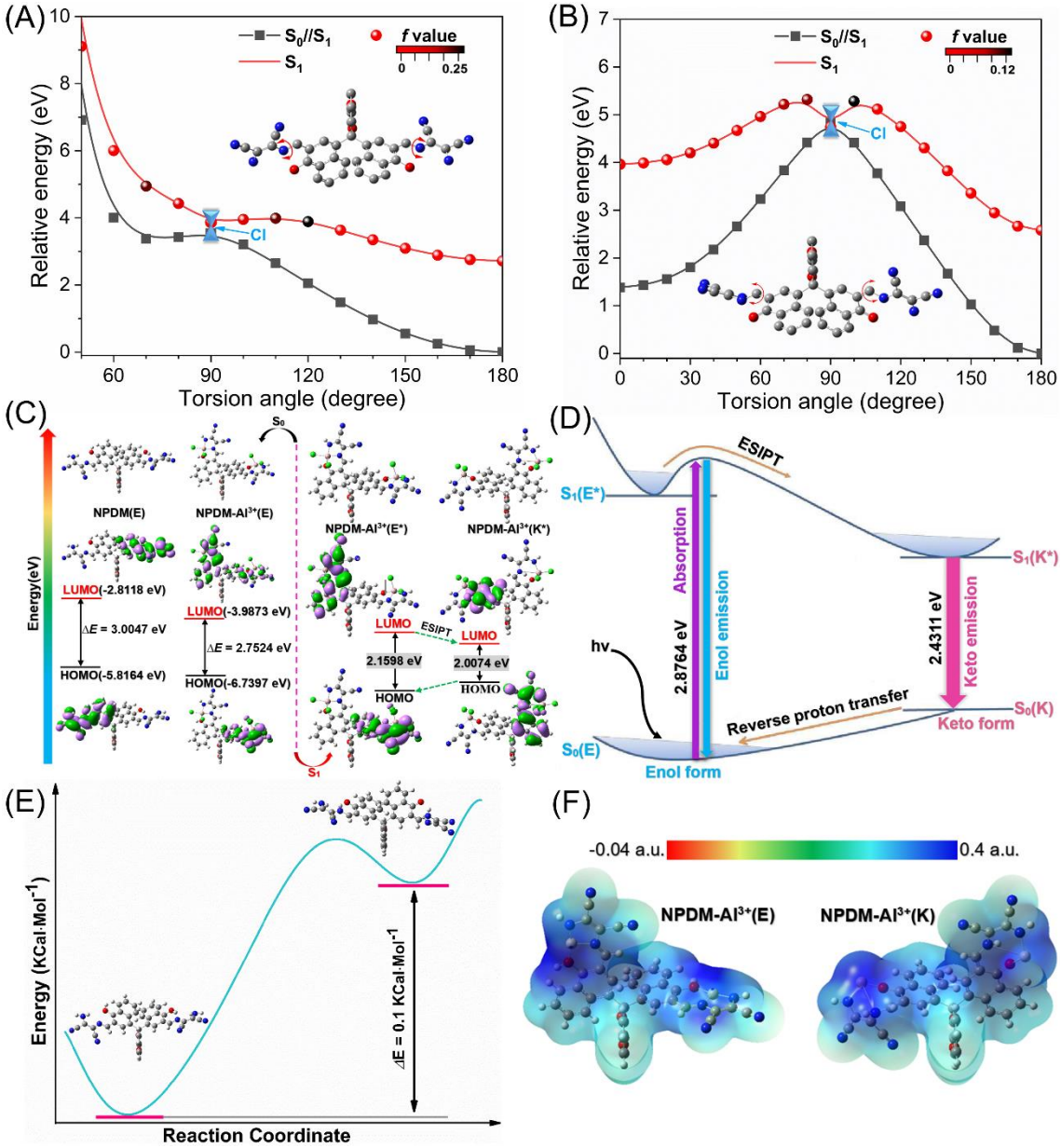

Fig. 3. The potential energy surfaces of **NPDM**(E*) (A) and **NPDM**(K*) (B) geometries in the excited state (S_1) as a function of the torsional angles using B3LYP/6-31G(d) method of TD-DFT calculations. $S_0//S_1$ is the ground state (S_0) projected vertically by S_1. (C) (TD)DFT calculated molecular orbitals and energy levels of ground and excited-state **NPDM** and **NPDM**-Al^{3+} complex in the forms of *enol* and *keto* (B3LYP/6-31G*/Lanl2dz levels). (D) Energy level diagram for **NPDM**-Al^{3+} and proposed photophysical process (ESIPT process). (E) The relative Gibbs free energy (kcal/mol) of **NPDM**(E) and **NPDM**(K). (F) Electrostatic potential (ESP) maps for **NPDM**-Al^{3+}(E) and **NPDM**-Al^{3+}(K) in S_0 state (B3LYP/6-311G** level).

the vibrational relaxations to their original S_0 states or isomers.[108] The total de-excited processes are defined as PIND. It is noteworthy that the excited **NPDM** molecule (E* and K*) exhibits the double bond twisting behaviors, resulting in the vain overlap of molecular orbitals with $f = 0$ in the emissive transitions, which caused that the **NPDM** molecule has almost no fluorescence in RT solution. Thus, the rotations of double-bond could explain the special emission behaviors of the tweezers **NPDM**. Obviously, the weak emissions of **NPDM** in aqueous DMSO were mainly owing to the ease of C=N bond/C=C bond rotation in the S_1 states. When configurational change between E* and K* forms occurred, the CI would be clearly found in the PES plots. **NPDM** alone shows negligible emissions in aqueous DMSO solution, however, **NPDM**-Al^{3+} complex

shows dramatic fluorescence enhancement because the double bond twisting behaviors within the molecules were blocked and the C=N isomerization is limited.[123] Briefly, the exciton could be released dominantly through radiative decay resulting in the strong fluorescence emissions. These explained why the emissions of **NPDM** alone were much weaker in aqueous DMSO.

To strengthen the interaction mechanism, the optimized geometries and the HOMO/LUMO orbital energies of **NPDM**, and **NPDM**-Al^{3+} (enol-keto forms) were again computed using (TD)DFT calculations through Gaussian 09[124] (Fig. 3C, Fig. S15). The energy gaps of **NPDM**, and **NPDM-**Al^{3+} in the S_0 states were examined as 3.0047 eV, and 2.7524 eV respectively. The data show that the binding of Al^{3+} to **NPDM** narrowers the energy gap and stabilizes the system, also confirming the red-shift of **NPDM-**Al^{3+} in the absorption maxima, which coincides well with the aforementioned absorption spectra analysis. Additionally, the energy gaps of **NPDM**-Al^{3+} complex (E*) and **NPDM**-Al^{3+} complex (K*) were determined to be 2.1598 eV and 2.0074 eV, respectively. These calculations demonstrated that the energy gaps in the **NPDM**-Al^{3+} complexes (E*- K* forms) were quite lower than that of **NPDM**, verifying the enhancement of ICT effect. Furthermore, the energy gap of **NPDM**-Al^{3+} complex (E*) was larger than that of **NPDM**-Al^{3+} complex (K*), which could be responsible for dual emissions of **NPDM**-Al^{3+} because of ESIPT process.

In addition, the TD-DFT calculations were also performed to describe the specific ESIPT luminescence mechanism observed above (Fig. 3D, Table S2 ESI). The computational vertical excitation energy in the S_0(E) → S_1(E*) process is 2.8764 eV (431 nm), approximate to the absorption peak value of **NPDM-**Al^{3+} in solution (436 nm). The vertical emission energy in the S_1(K*) → S_0(K) was calculated as 2.4311 eV (510 nm), approximating the emission peak value of **NPDM-**Al^{3+} in keto form (556 nm). There is not a local minimum for S_0(K), hence **NPDM-**Al^{3+} returns to S_0(E) without energy barrier (Fig. 3D).[125] With the aid of the theoretical calculations, the photophysical process of **NPDM**-Al^{3+} has been elucidated (Fig. 3D). In the electronic S_0 state, **NPDM**-Al^{3+} exists solely as a S_0(E) form like other quintessential ESIPT molecules for the steady intramolecular H-bonds. Upon photoexitation, S_1(E*) was transformed into tautomer S_1(K*) through an ultrafast ESIPT process,[126] which caused the transient change of the electronic characteristics and simultaneously the formation of a new S_1 state PES.[127] After decaying radiatively to S_0(K), followed by reverse proton transfer process happened to the original S_0(E) form, eventually finishing the ESIPT photocycle. The above studies were better enough to understand the ESIPT mechanism of tweezers **NPDM** towards Al^{3+}.

Generally, the thermodynamic parameters can assess the rationality of numerous chemical reaction pathways. Thus, the free energies of the transformation systems were calculated at the B3LYP/6-31G(d,p) level in DMSO-H_2O, using the IEFPCM model.[128] The results revealed that the Gibbs free energy of **NPDM**(K) is 0.1 kcal/mol higher than that of the **NPDM**(E) (Fig. 3E), proving that this transfer process is an exothermic reaction, which is thermodynamically favorable from the **NPDM**(K) to **NPDM**(E). In further

investigation of the luminous mechanism, the ESP maps were performed to interpret the charge distribution difference between **NPDM**-Al^{3+}(E) and **NPDM**-Al^{3+}(K). As shown in Fig. 3F, the ESP values of **NPDM**-Al^{3+}(E) and **NPDM**-Al^{3+}(K) are positive across the whole molecular scaffolds, demonstrating the inhibition of PET effect in **NPDM**-Al^{3+}, which are consistent with the above spectral analysis. These results consolidated our proposed response mechanism (Scheme 1).

2.5 Molecular memory device

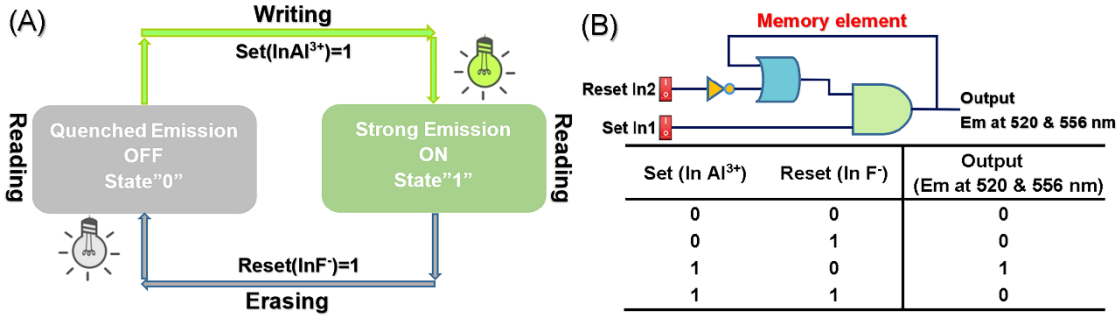

Set (In Al^{3+})	Reset (In F^-)	Output (Em at 520 & 556 nm)
0	0	0
0	1	0
1	0	1
1	1	0

Fig. 4. (A) Feedback loop showing the reversible logic operations for the memory element with "Reading-Erasing-Reading-Writing" functions. (B) The sequential logic circuit of the memory machine and its truth table.

Molecular logic gate is an interdisciplinary research field, and many efforts have been made to design molecular memory device in recent years.[129,130] Sequential logic circuits are significant for the making of molecular memory devices to store data and execute logic gate operation via feedback loops, in which one of the outputs functions as an input of the memory device and is memorized as a 'memory element'.[131] Inspired by the above observations, we designed a sequential logic circuit that displayed a 'Reading-Writing-Erasing-Reading' property assisted by a binary logic function (Fig. 4). In the concrete system, we chose dual strong fluorescence outputs at 520 and 556 nm as the 'ON' state (Output = 1) and two quenched emission outputs as the 'OFF' state (Output = 0). Here, the two chemical inputs, namely Al^{3+} (1) and F^- (2), were chosed for the Set (S) and Reset (R) processes, respectively, and their existance is considered as "1" and the absence is designated as "0". The operation of this memory function is as follows:[132,133] when the S input is a dual high emission values (S = 1), the system writes and then memorizes the binary state "1". By using R input (R=1), the stored data is erased, and then the binary state "0" will be memorized with the dual emissions quenching dramatically. Fig. 4A depicts the bistable behavior, 'OFF-ON' state, of the tweezers **NPDM** and discloses the non-volatile feature of the "memory effect". The behavior can be popularly used in microprocessors for memory cells of integrated logic circuits.[134,135] As described in Fig. 4B, this type of repeatable and reconfigurable sequences of S/R logic operations can be embodied in the shape of a feedback loop, which manifests a memory nature akin to 'Reading-Writing-Erasing-Reading' functions. It is noteworthy that the logic device as presented here demonstrates its large advantages over early developed related systems, at least in relation to the reversibility and reproducibility as well as the great potentials for successive determination

of common metal ions and anions (F^-).

2.6 Biological imaging

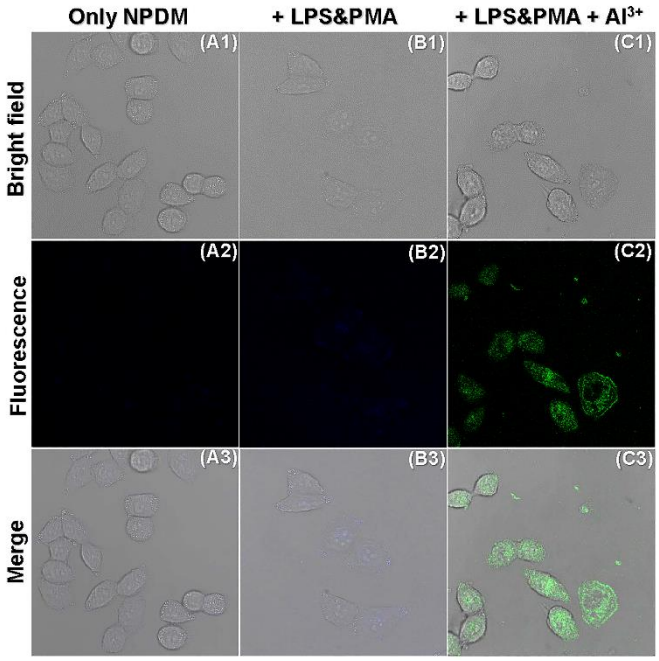

Fig. 5. Confocal fluorescence images of cells. HeLa cells were only treated with (A) **NPDM** (10 μM) for 0.5 h; (B) LPS (2 μg/mL), and PMA (2 μg/mL) for 4 h, and then **NPDM** for 0.5 h; (C) LPS (2 μg/mL) for 4 h, and PMA (2 μg/mL) and **NPDM** (10 μM) for 1 h, and then Al^{3+}(30 μM) for 0.5 h. Fluorescence channel: blue channel (420-490 nm), λ_{ex} = 405 nm; green channel (500-550 nm), λ_{ex} = 488 nm. Scale bar: 50 μm.

The above results enunciated the eminent sensing performance of **NPDM** towards Al^{3+} in solution, then again, the MTT assay showed that **NPDM** has very low cytotoxicity even at high concentrations (Fig. S16, ESI). In view of the redox-active Schiff-base-based fluorogenic probes can easily suffer from oxygenolysis which was induced by reactive oxygen species (ROS) and reactive nitrogen species (RNS), such as OCl^-, $ONOO^-$, and H_2O_2, which are three primary ROS and RNS in live cells, and evidence also suggests that OCl^- and $ONOO^-$ can affect the fluorescence changes by oxidizing the C=N moiety of DAMN-based Schiff-base luminophores,[107,136,137] the chemical stability of **NPDM** for Al^{3+} detection in living cells was also investigated by evaluating the resistance to endogenous OCl^- and $ONOO^-$. As shown in Fig. 5A, when the cells were treated with **NPDM** alone, there was almost none fluorescence signal. Then, lipopolysaccharide (LPS) and PMA were used to stimulate cells produce endogenous $ONOO^-$ and OCl^-. However, no fluorescence signal was observed in the green channel but the cells showed ignorable fluorescence signal in the blue channel when the cells were pretreated with LPS and PMA for 4 h, and then stained with **NPDM** for 0.5 h (Fig. 5B). Next, the cells further cultured with Al^{3+} showed obvious green fluorescence (Fig. 5C), indicating the excellent chemical stability of **NPDM** in living cells. All the results clearly manifested that **NPDM** is capable of long-term tracing Al^{3+} without interferences by active substances in living cells.

With these results in hand, we further checked the traceability of **NPDM** to monitor Al^{3+} in live HeLa cells

(Fig. 6A). Firstly, the Hela cells treated with **NPDM** alone showed no fluorescence signal in the green channel, while Hela cells were pre-incubated with **NPDM** and co-cultured with ascending Al^{3+}, and the increasing green fluorescence signals were observed (Fig. 6D). Thus, the above cell imaging results showed that **NPDM** could monitor Al^{3+} in living cells with favourable cell penetrability and sufficient sensitivity.

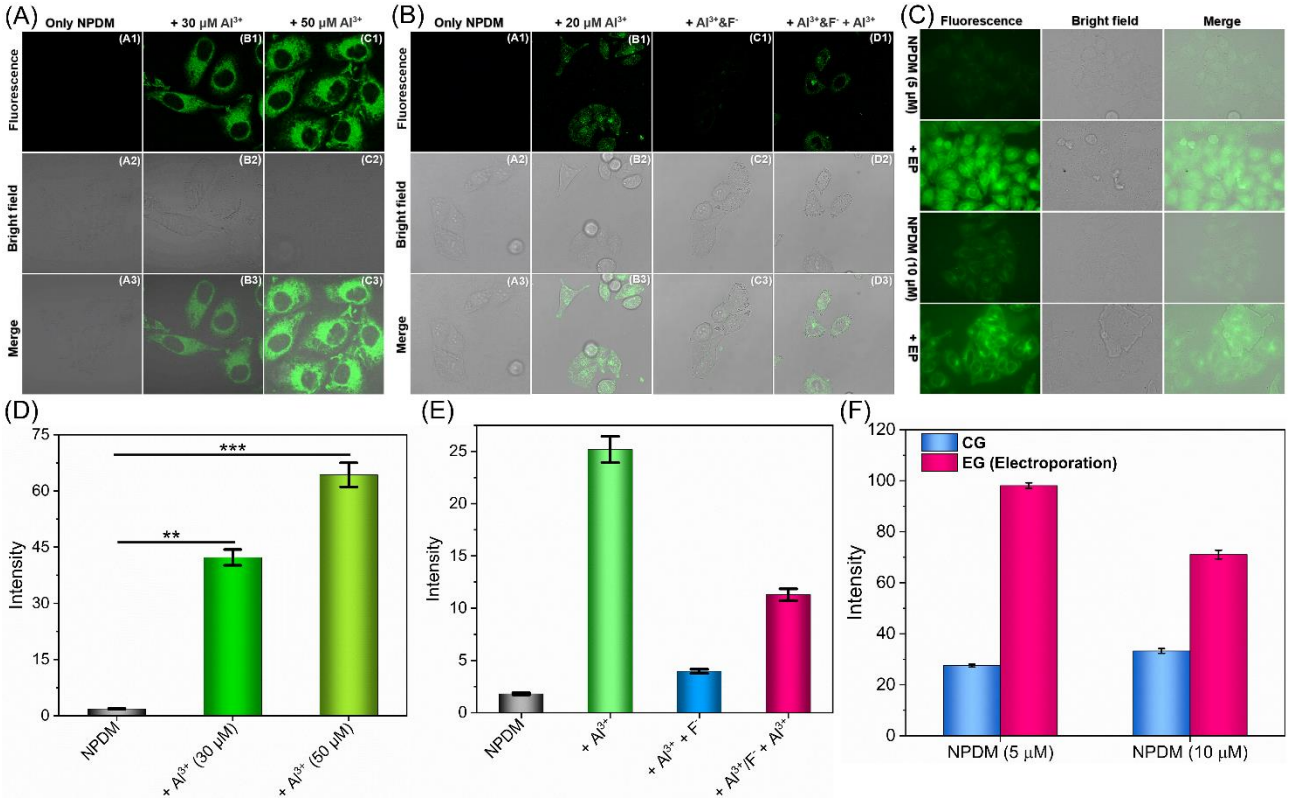

Fig. 6. Confocal microscopy fluorescence images of living HeLa cells: (A) The cells incubated only with **NPDM** (10 μM) for 20 mins as the control group (A1-A3); the cells preincubated with **NPDM** for 20 mins and then incubated with 30 μmol/L Al^{3+} (B1-B3) and 50 μmol/L Al^{3+} (C1-C3); Scale bar: 20 μm. (B) Incubated 10 μM of **NPDM** for 20 min (A1-A3); Incubated with **NPDM** (10 μM) for 20 min and then treated with Al^{3+} (20 μM) (B1-B3); Incubated with **NPDM** (10 μM) and Al^{3+} (20 μM) and then exposed to F^- (40 μM) (C1-C3); Incubated with **NPDM** (10 μM), Al^{3+} (20 μM), and exposed to F^- (40 μM), and then treated with Al^{3+} (80 μM) (D1-D3); Scale bar: 50 μm. Fluorescence microscopy imaging: (C) HeLa cells incubated only with **NPDM** (5 μM) for 20 mins as the control group; Cells subjected to electric shock, and then incubated with **NPDM** (5 μM); HeLa cells incubated only with **NPDM** (10 μM) for 20 mins as the control group; Cells subjected to electric shock, and then incubated with **NPDM** (10 μM); electric shock frequency: 3. Fluorescence channel: green channel (500-550 nm), λ_{ex} = 488 nm. Bar graph: (D) Average fluorescence intensity of Al^{3+} green channel, **p < 0.01, ***p < 0.001 (n = 3). (E) Fluorescence intensity of Al^{3+} green channel with separate **NPDM** and different F^- concentration. (F) Fluorescence intensity of green channel in each group (**NPDM**: 5, 10 μM).

To further verify the recyclability of **NPDM** in living biosamples, another fluorescence-imaging experiments were carried in HeLa cells (Fig. 6B). As the cells were treated with only **NPDM**, there were no any fluorescence signal in the green channel. When HeLa cells were further treated with 2 equivalent Al^{3+}, the bright green fluorescence was observed. Furthermore, addition of the 4 equivalent F^- quenched the green fluorescence. Attractively, followed by addition of the excessive Al^{3+} (appr. 80 μM) restored the intense green fluorescence (Fig. 6E). The alterations of intracellular fluorescence was in good accordance with the

phenomena in solution. The above phenomena showed that tweezers **NPDM** can act as a reliable tool to sequentially monitor Al^{3+} and F^- level in live cells, revealing reversible imaging property of tweezers **NPDM** in living cells.

In traditional cell electroporation experiments, we often use aluminum electrodes, but which can lead to leaking of Al^{3+} ions, causing cells damage. Taking this into account, we try to employ tweezers **NPDM** in detecting the Al^{3+} formed during the electric shock process. As shown in Fig. 6C, before the electric shock, as the cells were treated with **NPDM**, there were faint fluorescence signals in the green channel, while the obvious green fluorescences were observed after the cells were subjected to an electric shock. Intriguingly, the green fluorescence signal in the group of low **NPDM** concentration is stronger than that in the group of high **NPDM** concentration (Fig. 6F), which can be attributed to the bistructure of tweezers **NPDM**. Therefore, it is better to use conductive polymer electrodes than that of the aluminum electrodes to maintain cellular homeostasis and promote cell survival. Noteworthily, it is the first reported smart tweezers capable of verifying the leaking behavior of Al^{3+} ions during electroporation, which is beneficial to select suitable electroporation electrode materials in future electroporation researches.

2.7 Practical application studies

In general, during the detection, we can directly observe the fluorescence color alterations with naked eyes assisted by UV light. Nevertheless, the semiquantitative detection can not be achieved with this method, and the result possibly can have the personal error.[16,138-140] Thus, to overcome these limitations and to access the satisfactory detection accuracy and reliability, a smartphone-assisted intelligent sensing platform was built based on the fluorogenic tweezers **NPDM**. All the fluorogenic photo colors from prepared samples (solutions and cotton swabs) were captured, and then converted them into the precise readable digital information and outputed the results (RGB values) using the APP *ColorAsisst* by employing the portable smartphone (Fig.7A). In solution-phase, the relationship between the R/G ratio of the fluorescence color alterations and added Al^{3+} concentration (0~10 μM) has linearity ($R^2 = 0.9686$) (Fig. S17, ESI). The LOD of the RGB method was found to be 82.8 nM. But the fly in the ointment was that the linearity was unsatisfactory. Thus, to improve the linearity of the RGB assay, the solide-phase samples (cotton swab as the support) were prepared. Fig. 7B shows that the fluorescence color was changed from green to yellow as compared with that in the solution, and a reliable and better linear relationship ($R^2 = 0.98$) between the R/G value and the Al^{3+} concentration (0~30 μM) was presented, and the LOD of the RGB platform was 45.4 nM, which confirmed the superiority of the solid-state interface over a liquid surface. Although this method is imperfect at present, our RGB platform constructed by fluorogenic tweezers **NPDM** and smartphone provides a promising analytical strategy for the portable, semiquantitative, rapid, simple, and in-field visual detection of Al^{3+} and other analytes without any

complicated and costly apparatus, which is especially suitable for the deprived areas. Thus, as the abstracted unknown sampled signals are introduced to the standard calibration curve, semiquantitative assessment of unknown samples could be ascertained appropriately. In this way, quick and precise assessment of the unknown samples could be obtained through integrating together and phototaking procedures utilizing a smartphone with wide field applications (Fig. 7C).[141]

Aiming to further examine the practicality and reliability of the integrated sensing platform, we utilized the as-proposed method for sensing Al^{3+} in real samples (the environment water samples, tea, Chinese wolfberry and milk powder), like river water, bay water, tap water, and green tea. As shown in Table S3 (ESI), the recoveries of Al^{3+} ranged from 91.07 % to 102.04 % with the low relative standard deviation (RSD) below 5 %, implying that this portable RGB system based on tweezers **NPDM** is fully competent for *in-field* sensing Al^{3+} with the high reliability and accuracy in environmental water and food samples. The above results conclude that the intelligent sensing platform has great latent capacity and feasibility for the semiquantitative determination of Al^{3+} in real samples.

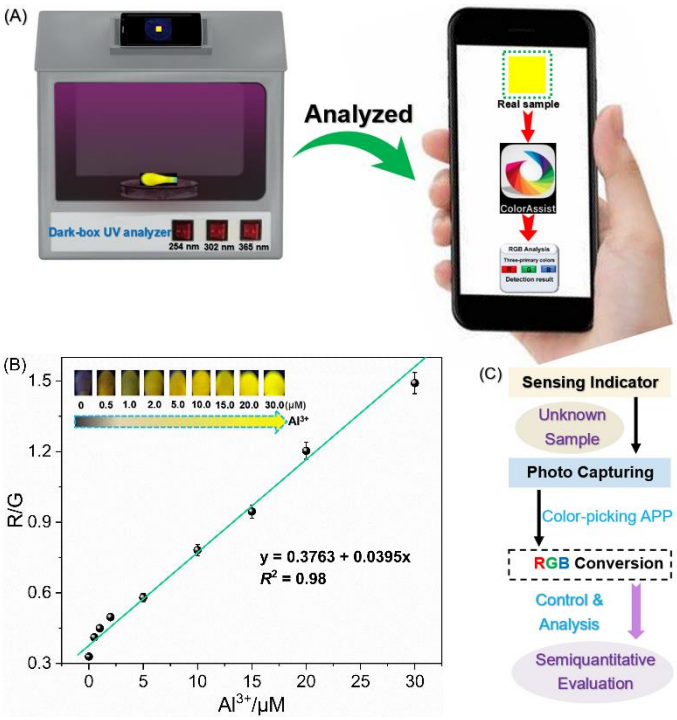

Fig. 7. (A) Illustrations of the smartphone-assisted platform for Al^{3+} detection: RGB value of the fluorescence samples outputted from the *ColorAssist* applet of the smartphone. (B) The linear relationship between the R/G ratio and [Al^{3+}] (0~30 μM) (inset: the fluorescence change photograph of **NPDM**-impregnated cotton swabs sprayed with the various concentration of Al^{3+} (0 μM, 0.5 μM, 1.0 μM, 2.0 μM, 5.0 μM, 10.0 μM, 15.0 μM, 20.0 μM, 30 μM) recording with smartphone-assisted platform. Error bars represent standard deviations (n=3). (C) Scheme illustrating the whole processes of sample evaluation by portable analyzer in field applications.

3. Conclusions

In summary, a novel ESIPT-active α-naphtholphthalein-DAMN hydrazone **NPDM** was successfully

developed for enhanced identification specificity and efficiency toward Al^{3+}. Molecular tweezers **NPDM** for Al^{3+} sensing via ESIPT and CHEF mechanisms, demonstrates merits of dual emissions, splendid selectivity and sensitivity with a very low LOD of 16.3 nM, large Stokes shifts (140 nm/176 nm), and real-time and visualized sensing. The Job's plot, HRMS, ^1H NMR titrations, as well as detailed (TD)DFT calculations elucidated the formation of a 1:2 **NPDM**-Al^{3+} complex with ESIPT "turn-on" process. Intriguingly, **NPDM**-Al^{3+} ensemble can also be utilized as a subsequent fluorescence tweezers for the selective and sensitive recognition of F^- anions. Basing on this reversible sensing property, an advanced molecular memory device was fabricated. Moreover, benefiting from the excellent optical performances and biocompatibility, **NPDM** was efficiently applied in imaging the intracellular Al^{3+} and F^- ions in Hela cells with good resistance to oxidative stress, especially the OCl^- and $ONOO^-$ species. More importantly, it is the first reported smart tweezers capable of detecting the Al^{3+} ions formed during electroporation. Also to assess its practical applications value, a smartphone-integrated intelligent platform was successfully built and applied to detect Al^{3+} in water samples, and satisfactory recoveries were attained, which powerfully proved that **NPDM** possesses a great practical potential for the visual detection of Al^{3+} in environmental samples with the advantages of portability, simplicity, rapidity, low cost, and on-site sensing. Hence, according to the present results, we believe that more efforts can be devoted to the progress of ESIPT-active fluorogenic tweezers and helped to extend their practical application areas in the subsequent study.

Author contributions

Daoyong Jiang: conceptualization, data curation, investigation, writing–original draft, writing–review & editing. Tingfei Xie: data curation, investigation, writing–original draft, writing–review & editing. Yizhao Chen: data curation, writing–original draft, validation, writing–review & editing. Xiuwen Zhang: investigation, methodology, writing –review & editing. Jihong Chen: investigation, methodology, writing –review & editing. Xiaowei Qi: investigation, methodology, writing –review & editing. Pengfei Zhang: conceptualization, funding acquisition, supervision, writing–review & editing. and Yong Wang: conceptualization, funding acquisition, writing–review & editing.

All authors revised and approved the text.

Conflicts of interest

There are no conflicts to declare.

Acknowledgements

This work was partially supported by the National Natural Science Foundation of China (82460364 and 81901906), National Key R&D Program (2021YFA0910000), the Shenzhen Science and Technology Program

(KQTD20210811090115019), the Shenzhen basic research (key project) (JCYJ20210324120011030 and JCYJ20210324115804013), the Postdoctoral Initiation Program Foundation (4105-6020330011K0), Guangdong Basic and Applied Basic Research Fund Project (2019A1515110222), Zhuhai innovation and entrepreneurship team project (ZH01110-405180056PWC), and the Innovation and Technology Commission (MHP/047/19) and the Major Instrumentation Development Program of the Chinese Academy of Sciences (ZDKYYQ20220008).

Notes and references

1 H. Wan, Q. Xu, P. Gu, H. Li, D. Chen, N. Li, J. He, J. Lu, *J. Hazard. Mater.* **2021**, *403*, 123656.

2 T. Rasheed, C. Li, M. Bilal, C. Yu, H. M. Iqbal, *Sci. Total Environ.* **2018**, *640*, 174-193.

3 H. M. Junaid, M. Batool, F. W. Harun, M. S. Akhter, N. Shabbir, *Crit. Rev. Anal. Chem.* **2022**, *52*, 463-480.

4 R. AbhijnaKrishna and S. Velmathi, *Coordin. Chem. Rev.* **2022**, *459*, 214401.

5 A. L. Berhanu, I. Mohiuddin, A. K. Malik, J. S. Aulakh, V. Kumar, K.-H. Kim, *Trends Anal. Chem.* **2019**, *116*, 74-91.

6 P. J. Roy, *Dalton Trans.* **2021**, *50*, 7156-7165.

7 J. Wang, H. Xie, H. Li, R. Wang, B. Zhang, T. Ren, J. Hua, N. Chen, *J. Agric. Food Chem.* **2021**, *69*, 14330-14339.

8 A. R. U. Parambil, P. Kavyashree, A. Silswal, A. L. Koner, *RSC Adv.* **2022**, *12*, 13950-13970.

9 J. C. Berrones-Reyes, B. M. Muñoz-Flores, M. A. Treto-Suárez, Y. Hidalgo-Rosa, E. Schott, D. Páez-Hernández, P. M. Gurubasavaraj, X. Zarate, V. M. Jiménez-Pérez, *Eur. J. Org. Chem.* **2022**, *37*, e202200588.

10 C. I. David, G. Prabakaran, R. J. Nandhakumar, *Microchem. J.* **2021**, *169*, 106590.

11 K. Pomazal, C. Prohaska, I. Steffan, G. Reich, J. F. K. Hube, *Analyst* **1999**, *124*, 657-663.

12 J. E. T. Andersen, *Analyst* **2005**, *130*, 385-390.

13 B. Avula, Y.-H. Wang, T. J. Smillie, N. S. Duzgoren-Aydin, I. A. Khan, *J. Agric. Food Chem.* **2010**, *58*, 8887-8894.

14 M. N. El-Nahass, T. A. Fayed, H. A. El-Daly, M. M. Youssif, *Appl. Organomet. Chem.* **2022**, *36*, e6703.

15 X. Liu, Y. Yao, Y. Ying, J. Ping, *Trends Anal. Chem.* **2019**, *115*, 187-202.

16 F. Yang, D. Lin, L. Pan, J. Zhu, J. Shen, L. Yang, C. Jiang, *Anal. Chem.* **2021**, *93*, 14506-14513.

17 L. Han, Y. Z. Fan, M. Qing, S. G. Liu, Y. Z. Yang, N. B. Li, H. Q. Luo, *ACS Appl. Mater. Inter.* **2020**, *12*, 47099-47107.

18 S. Y. Chu, H. Q. Wang, X. Ling, S. M. Yu, L. Yang, C. L. Jiang, *ACS Appl. Mater. Inter*. **2020**, *12*, 12962-12971.

19 S. Tang, D. Chen, G. Guo, X. Li, C. Wang, T. Li, G. Wang, *Sci. Total Environ.* **2022**, *825*, 153913.

20 L. Guo, S. Chen, Y.-L. Yu, J.-H. Wang, *Anal. Chem.* **2021**, *93*, 16240-16247.

21 X. Chen, X. Wang, Y. Fang, L. Zhang, M. Zhao, Y. Liu, *Anal. Chem.* **2022**, *94*, 8382-8391.

22 X. Yuan, F. Bai, H. Ye, H. Zhao, L. Zhao, Z. Xiong, *Anal. Chim. Acta* **2021**, *1188*, 339165.

23 N. Duan, H. Wang, Y. Li, S.Yang, H. Tian, J. B. Sun, *Coord. Chem. Rev.* **2021**, *427*, 213557.

24 D. Cao, Z. Liu, P. Verwilst, S. Koo, P. Jangjili, J. S. Kim, W. J. Lin, *Chem. Rev.* **2019**, *119*, 10403-10519.

25 S.-H. Park, N. Kwon, J.-H. Lee, J. Yoon, I. J. Shin, *Chem. Soc. Rev.* **2020**, *49*, 143-179.

26 N. Duan, S. Yang, H. Tian, B. Sun, *Food Chem.* **2021**, *358*, 129839.

27 X. Huang, R. Zhang, C. Chen, R. T. Kwok, B. Z. Tang, *Mater. Chem. Front*. **2021**, *5*, 723-743.

28 P. Zhang, Q. Zhang, L. Zhang, H. Zhong, C. Ding, *Trends Anal. Chem.* **2020**, *123*, 115776.

29 J. Chan, S. C. Dodani, C. J. Chang, *Nat. Chem.* **2012**, *4*, 973-984.

30 X. P. Yang, D. Zhang, Y. Ye, Y. F. Zhao, *Coord. Chem. Rev.* **2022**, *453*, 214336.

31 K. J. Bruemmer, S. W. M. Crossley, C. J. Chang, *Angew. Chem. Int. Ed*. **2020**, *59*, 2-31.

32 S. K. Pramanik, A. Das, *Chem. Commun*. **2021**, *57*, 12058-12073.

33 S. Singha, Y. W. Jun, S. Sarkar, K. H. Ahn, *Acc. Chem. Res*. **2019**, *52*, 2571-2581.

34 A. Gupta, N. Kumar, *RSC Adv.* **2016**, *6*, 106413-106434.

35 R. A. Yokel, *Coord. Chem. Rev.* **2002**, *228*, 97-113.

36 H. Li, H. Kim, J. Han, V.-N. Nguyen, X. Peng and J. Yoon, *Aggregate* **2021**, *2*, e51.

37 M. Kang, Z. Zhang, N. Song, M. Li, P. Sun, X. Chen, D. Wang, B. Z. Tang, *Aggregate* **2020**, *1*, 80-106.

38 M. H. Chua, H.Zhou, Q. Zhu, B. Z. Tang, J. W. Xu, *Mater. Chem. Front.* **2021**, *5*, 659-708.

39 P. Zhou and K. Han, *Acc. Chem. Res.* **2018**, *51*, 1681-1690.

40 X.-L. Lu, W. HE, *Chinese J. Anal. Chem.* **2021**, *49*, 184-196.

41 Z.-L. Che, C.-C. Yan, X.-D. Wang, L.-S. Liao, *Chin. J. Chem.* **2022**, *40*, 2468-2481.

42 R. Wang, X. Lai, G. Qiu, J. Liu, *Chin. J. Org. Chem.* **2019**, *39,* 952-960.

43 W. Sun, M. Li, J. Fan, X. Peng, *Acc. Chem. Res.* **2019**, *52*, 2818-2831.

44 B. Daly, J. Ling, A. P. de Silva, *Chem. Soc. Rev.* **2015**, *44*, 4203-4211.

45 C. S. Abeywickrama, *Chem. Commun.* **2022**, *58*, 9855-9869.

46 A. Pal, M. Karmakar, S. R. Bhatta and A. Thakur, *Coordin. Chem. Rev.* **2021**, *448*, 214167.

47 J. Wang, Q. Meng, Y. Yang, S. Zhong, R. Zhang, Y. Fang, Y. Gao, X. Cui, *ACS Sens*. **2022**, *7*, 2521-2536.

48 L. Patra, S. Das, S. Gharami, K. Aich, T. K. Mondal, *New J. Chem.* **2018**, *42*, 19076-19082.

49 L. Wu, C. Huang, B. P. Emery, A. C. Sedgwick, S. D. Bull, X.-P. He, H. Tian, J. Yoon, J. L. Sessler, T. D. James, *Chem. Soc. Rev.* **2020**, *49*, 5110-5139.

50 W. Zhang, X. Liu, P. Li, W. Zhang, H. Wang, B. Tang, *Trends Anal. Chem.* **2020**, *123*, 115742.

51 Y. Wang, Y. Bian, X. Chen, D. Su, *Chem Asian J.* **2022**, *17*, e202200018.

52 U. Haris, H. N. Kagalwala, Y. L. Kim, A. R. Lippert, *Acc. Chem. Res.* **2021**, *54*, 2844-2857.

53 M. Yang, J. Huang, J. Fan, J. Du, K. Pu, X. Peng, *Chem. Soc. Rev.* **2020**, *49*, 6800-6815.

54 L. Zhou, X. Zhang, Q. Wang, Y. Lv, G. Mao, A. Luo, Y. Wu, Y. Wu, J. Zhang, W. Tan, *J. Am. Chem. Soc.* **2014**, *136*, 9838-9841.

55 W. Lin, L. Yuan, Z. Cao,Y. Feng, J. Song, *Angew. Chem., Int. Ed.* **2010**, *49*, 375-379.

56 G. Wang, Z. Wan, Z. Cai, J. Li, Y. Li, X. Hu, D. Lei, X. Dou, *Anal. Chem.* **2022**, *94*, 11679-11687.

57 A. C. Sedgwick, L. Wu, H.-H. Han, S. D. Bull, X.-P. He, T. D. James, J. L. Sessler, B. Z.Tang, H. Tian, J. J. Yoon, *Chem. Soc. Rev*. **2018**, *47*, 8842-8880.

58 P. Zhou, K. Han, *Aggregate* **2022**, *3*, e160.

59 M. H. Lee, J. S. Kim, J. L. Sessler, *Chem. Soc. Rev.* **2015**, *44*, 4185-4191.

60 X. Liu, A. Li, W. Xu, Z. Ma, X. Jia, *Mater. Chem. Front.* **2019**, *3*, 620-625.

61 A. C. Sedgwick, W.-T. Dou, J.-B. Jiao, L. Wu, G. T. Williams, A. T. A. Jenkins, S. D. Bull, J. L. Sessler, X.-P. He, T. D. James, *J. Am. Chem. Soc.* **2018**, *140,* 14267-14271.

62 H. Hu, X. Cheng, Z. Ma, R. P. Sijbesma, Z. Ma, *J. Am. Chem. Soc.* **2022**, *144*, 9971-9979.

63 L.-J. Yan, C. Jiang, A.-Y. Ye, Q. He, C. Yao, *Spectrochim. Acta. A* **2022**, *268*, 120639.

64 Y. He, J. Yu, X. Hu, S. Huang, L. Cai, L. Yang, H. Zhang, Y. Jiang, Y. Jia, H. Sun, *Chem. Commun.* **2020**, *56*, 13323-13326.

65 S. Samanta, U. Manna, G. Das, *New J. Chem.* **2017**, *41*, 1064-1072.

66 H. Ren, F. Huo, C. Yin, *New J. Chem.* **2021**, *45*, 4724-4728.

67 R. Ali, R. C. Gupta, S. K. Dwivedi, A. Misra, *New J. Chem.* **2018**, *42*, 11746-11754.

68 Q. Deng, K. Ding, Y. Li, Y. Jiao, R. Hu, T. Zhang, Z. Wang, B. Z. Tang, *Biomaterials* **2022**, *289*, 121767.

69 R. Hu, Q. Deng, Q. Tang, R. Zhang, L. Wang, B. Situ, C. Gui, Z. Wang, B. Z. Tang, *Biomaterials* **2021**, *271*, 120725.

70 P. Puri, G. Kumar, K. Paul, V. Luxami, *New J. Chem.* **2018**, *42*, 18550-18558.

71 M. Mathivanan, B. Tharmalingam, O. Anitha, C.-H. Lin, V. Thiagarajan, B. Murugesapandian, *Mater. Chem. Front.* **2021**, *5*, 8183-8196.

72 F. Zhou, K. Zhang, G. Li, C. Gui, R. Hu, S. Li, Z. Wang, Y. Zhang, B. Z. Tang, *Mater. Chem. Front.* **2020**, *4*, 3094-3102.

73 L. Cui, Y. Baek, S. Lee, N. Kwon, J. Yoon, *J. Mater. Chem. C* **2016**, *4*, 2909-2914.

74 H. Song, Y. Zhou, H. Qu, C. Xu, X. Wang, X. Liu, Q. Zhang, X. Peng, *Ind. Eng. Chem. Res.* **2018,** *57*, 15216-15223.

75 J. Zhu, L. Lu , M. Wang, T. Sun, Y. Huang , C. Wang, W. Bao, M. Wang, F. Zou, Y. Tang , *Tetrahedron Lett.* **2020**, *61*, 151893.

76 Y. Li, C. Liao, S. S. Huang, H. Xu, B. Z. Zheng, J. Du, D. Xiao, *RSC Adv*. **2016**, *6*, 25420.

77 X.-Y. Kong, L.-J. Hou, X.-Q. Shao, S.-M. Shuang, Y. Wang, C. Dong, *Spectrochim. Acta A* **2019**, *208*, 131-139.

78 O. Alici, D. Aydin, *J. Photochem. Photobiol. A Chem*. **2018**, *359*, 172-182.

79 D. Aydin, M. K. Alici, *J. Fluoresc.* **2021**, *31*, 797-805.

80 D. Aydin, S. Dinckan, S. N. K. Elmas, T. Savran, F. N. Arslan, I. Yilmaz, *Food Chem*. **2021**, *337*, 127659.

81 A. Gul, M. Oguz, A. N. Kursunlu, M. Yilmaz, *Dyes Pigm*. **2020**, *176*, 108221.

82 X.-Y. Kong, S.-M. Shuang, Y. Wang, C. Dong, *Spectrochim. Acta A* **2022**, *276*, 121174.

83 Z. Qiao, Y. Wu, B. Tang, R. Perestrelo, R. Bhalla, *Tetrahedron Lett.* **2019**, *60*, 150918.

84 X.-L. Yue, Z.-Q Wang, C.-R. Li, Z.-Y. Yang, *Tetrahedron Lett.* **2017**, *58*, 4532-4537.

85 C. Balakrishnana, M. A. Neelakantana, S. Banerjee, *Sens. Actuators B Chem.* **2017**, *253*, 1012-1025.

86 S. Das, S. Goswami, K. Aich, K. Ghoshal, C. K. Quah, M. Bhattacharyya, H.-K. Fun, *New J. Chem.* **2015**, *39*, 8582-8587.

87 Y. Zhu, X. Gong, Z. Li, X. Zhao, Z. Liu, D. Cao, R. Guan, *Spectrochim. Acta A* **2019**, *219*, 202-205.

88 Q. Zheng, F. Ding, X. Hu, J. Feng, J. Shen, X. He, *Bioorg. Chem.* **2021**, *109*, 104746.

89 X. He, W. Xiong, L. Zhang, C. Xu, J. Fan, Y. Qian, J. Wen, F. Ding, J. Shen, *Dyes Pigm.* **2020**, *174*, 108059.

90 W. Pan, C. Zheng, G. Liao, G. Liu, S. Pu, *Microchem. J.* **2021**, *163*, 105887.

91 S. Erdemir and S. Malkondu, *Dyes Pigm.* **2019**, *163*, 330-336.

92 V. Kumar, A. Kumar, U. Diwan, R. Shweta, , S. K. Srivastava, K.K. Upadhyay, *Sens. Actuators B Chem.* **2015**, *207*, 650-657.

93 M. N. Amputu, J. Naimhwaka, V. Uahengo, *RSC Adv.* **2022**, *12*, 27022-27043.

94 H. Zhang, T. Sun, Q. Ruan, J.-L. Zhao, L. Mu, X. Zeng, Z. Jin, S. Su, Q. Luo, Y. Yan, C. Redshaw, *Dyes Pigm.* **2019**, *162*, 257-265.

95 D. Jiang, X. Xue, M. Zhu, G. Zhang, Y. Wang, C. Feng, Z. Wang, H. Zhao, *Ind. Eng. Chem. Res.* **2019**, *58*, 18456-18467.

96 M. H. Zhan, H. M. Jia, J. Y. Fan, H. M. Yu, E. Amador, W. Chen, *Anal. Chem.* **2019**, *91*, 6103-6110.

97 K. Keshava, P. Torawaneb, M. K. Kumawatd, K. Tayadeb, S. K. Sahooc, R. Srivastavad, A. Kuwar, *Biosens. Bioelectron*. **2017**, *92*, 95-100.

98 J. Tang, H.-Y. Yin, J.-L. Zhang, *Chem. Sci.* **2018**, *9*, 1931-1939.

99 H. Feng, Z. Zhang, Q. Meng, H. Jia, Y. Wang, R. Zhang, *Adv. Sci.* **2018,** *5*, 1800397.

100 J.-T. Hou, H. S. Kim, C. Duan, M. S. Ji, S. Wang, L. Zeng, W. X. Ren, J. S. Kim, *Chem. Commun.* **2019**, *55*, 2533-2536.

101 L. Chen, S. J. Park, D. Wu, H. M. Kim, J. Yoon, Pigments. *Dyes Pigm.* **2018**, *158*, 526-532.

102 Y. Zhang, L. Ma, C. Tang, S. Pan, D. Shi, S. Wang, M. Li, Y. Guo, *J. Mater. Chem. B* **2018**, *6*, 725-731.

103 H. Zhang, F. Huo, Y. Zhang, C. Yin, *Sens. Actuators B Chem.* **2018**, *269*, 180-188.

104 Y. Kang, Z. Liao, M. Wu, S. Li, D.-C. Fang, X.-J. Zheng, L.-P. Jin, *Dalton Trans.* **2018**, *47*, 13730-13738.

105 Z. Li, C. Liu, J. Wang, S. Wang, L. Xiao, X. Jing, *Spectrochim. Acta A* **2019**, *212*, 349-355.

106 Z. Li, J. Wang, L. Xiao, J. Wang, H. Yan, *Inorg. Chim. Acta* **2021**, *516*, 120147.

107 Y. Li, L. Liu, Y. Tang, Y. Wang, J. Han, L. Ni, *Spectrochim. Acta. A* **2020**, *232*, 118154.

108 J.-S. Ni, X. Zhang, G. Yang, T. Kang, X. Lin, M. Zha, Y. Li, L. Wang, K. Li, *Angew. Chem. Int. Ed.* **2020**, *59*, 11298-11302.

109 Y. Guo, F. Huo, C. Yin, J. Kang, J. F. Li, *RSC Adv.* **2015**, *5*, 10845-10848.

110 T. Saleem, S. Khan, M. Yaqub, M. Khalid, M. Islam, M. Y. ur Rehman, M. Rashid, I. Shafiq, A. A. C. Braga, A. Syed, A. H. Bahkali, J. F. Trant, Z. Shafiq, *New J. Chem.* **2022**, *46*, 18233-18243.

111 S. Liu, J. Lu, Q. Lu, J. Fan, L. Lin, C. Wang, Y. Song, *Front. Chem.* **2020**, *7*, 932.

112 Y. Cao, X. Yu, C. Sun, J. Cui, *Int. J. Mol. Sci.* **2022**, *23*, 2132.

113 P. Fu, Q. Yan, S. Wang, H. Wu, D. Cao, *New J. Chem.* **2022**, *46*, 12600-12608.

114 J. Han, J. Sun, Y. Li, Y. Duan, T. Han, *J. Mater. Chem. C* **2016**, *4*, 9287-9293.

115 F. Ren, P. Liu, Y. Gao, J. Shi, B. Tong, Z. Cai, Y. Dong, *Mater. Chem. Front.* **2019**, *3*, 57-63.

116 X. Feng, J. Zhang, Z. Hu, Q. Wang, M. M. Islam, J.-S. Ni, *J. Mater. Chem. C* **2019**, *7*, 6932-6940.

117 W. Luo, Z. Yuwen, H. Li, S. Pu, *New J. Chem.* **2022**, *46*, 2411-2422.

118 P. Porrawatkul, R. Pimsen, A. Kuyyogsuy, P. Nuengmatcha, *Orient. J. Chem.* **2018**, *34*, 188-195.

119 K. Dev, S. Singh, S. Bhardwaj, P. Kukreti, D. Ramakanth, P. Kumar, S. Saini, P. Roy, V. C. Srivastava, K. Ghosh, P. K. Maji. *Chem. Eur. J.* **2024**, *30*, e202403256.

120 S.M. Ng, M. Koneswaranb, R. Narayanaswamy, *RSC Adv.* **2016**, *6*, 21624-21661.

121 J. Liu, H. Zhang, L. Hu, J. Wang, J. W. Y. Lam, L. Blancafort, B. Z. Tang, *J. Am. Chem. Soc.* **2022**, *144*, 7901-7910.

122 J.-S. Ni, H. Liu, J. Liu, M. Jiang, Z. Zhao, Y. Chen, R. T. K. Kwok, J. W. Y. Lam, Q. Peng, B. Z. Tang, *Mater. Chem. Front.* **2018**, *2*, 1498-1507.

123 K. Zhong, H. Liu, S. Jin, X. Chen, *Dyes Pigm.* **2021**, *195*, 109714.

124 A. B. Davis, M. H. Ihde, A. M. Busenlehner, D. L. Davis, R. Mia, J. Panella, F. R. Fronczek, M. Bonizzoni, K. J. Wallace, *Inorg. Chem*. **2021**, *60*, 14238-14252.

125 S. Park, J. E. Kwon, S. Y. Park, O. H. Kwon, J. K. Kim, S. J. Yoon, J. W. Chung, D. R. Whang, S. K. Park, D. K. Lee, D. J. Jang, J. Gierschner, S. Y. Park, *Adv. Opt. Mater.* **2017**, *5*, 1700353.

126 B. Pettersson Rimgard, Z. Tao, G. A. Parada, L. F. Cotter, S. Hammes-Schiffer, J. M. Mayer and L. Hammarström, *Science* **2022**, *377*, 742-747.

127 P.-Y. Fu, B.-N. Li, Q.-S. Zhang, J.-T. Mo, S.-C. Wang, M. Pan, C.-Y. Su, *J. Am. Chem. Soc.* **2022**, *144*, 2726-2734.

128 D. Jiang, X. Xue, M. Zhu, G. Zhang, Y. Wang, C. Feng, Z. Wang, H. Zhao, *Ind. Eng. Chem. Res.* **2019**, *58*, 18456-18467.

129 S. Erbas-Cakmak, S. Kolemen, A. C. Sedgwick, T. Gunnlaugsson, T. D. James, J. Yoon, E. U. Akkaya, *Chem. Soc. Rev.* **2018**, *47*, 2228-2248.

130 L. Liu, L. Ga, J. Ai, *Biosens. Bioelectron.* **2022**, *213*, 114456.

131 D. Das, R. Alam, M. Ali, *Analyst* **2022**, *147*, 471-479.

132 Y.-M. Zhang, Y.-F. Li, K.-P. Zhong, W.-J. Qu, H. Yao, T.-B. Wei, Q. Lin, *New J. Chem.* **2018**, *42*, 16167-16173.

133 R. Alam, R. Bhowmick, A. S. M. Islam, A. katarkar, K. Chaudhuri, M. Ali, *New J. Chem.* **2017**, *41*, 8359-8369.

134 J. Liu, T. Zhang, X. Liu, J. W. Y. Lam, B. Z. Tang, Y. Chau, *Mater. Horiz.* **2022**, *9*, 2443-2449.

135 L. Q. Huang, J. Zhang, X. X. Yu, Y. F. Ma, T. J. Huang, X. Shen, H. Y. Qiu, X. X. He, S. C. Yin, *Spectrochim. Acta A* **2015**, *145*, 25-32.

136 C. Liang, W. Shu, R. Han, H. Kang, X. Zhang, J. Jing, R. Zhang, X. Zhang, *Spectrochim. Acta A* **2022**, *277*, 121264.

137 C. Wang, W. Shu, Q. Chen, C. Yang, S. Su, M. Gao, R. Zhang, J. Jing, X. Zhang, *Spectrochim. Acta A* **2021**, *260*, 119990.

138 R. Jiang, D. Lin, Q. Zhang, L. Li, L. Yang, *Sens. Actuators B Chem.* **2022**, *350*, 130902.

139 S. Rasheed, T. Kanwal, N. Ahmad, B. Fatima, M. Najam-ul-Haq, D. Hussain, *Trends Anal. Chem.* **2024**, *173*, 117640.

140 W. Fu, X. Fu, Z. Li, Z. Liu, X. Li, *Chem. Eng. J.* **2024**, *489*, 151225.

141 J. Zhao, K. Liu, R. Wang, T. Liu, Z. Wu, L. Ding, Y. Fang, *ACS Appl. Mater. Interfaces* **2022**, *14*, 53323-53330.

Graphical abstract:

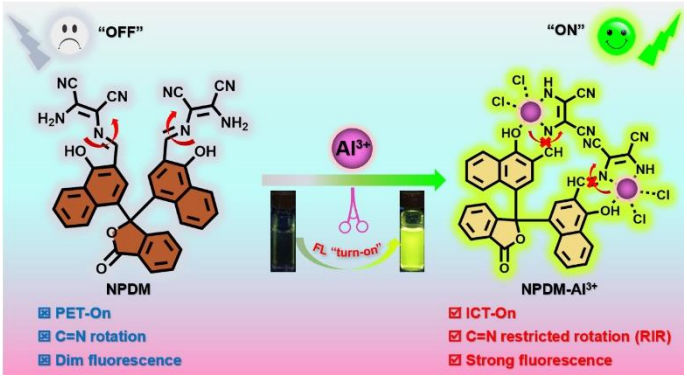

An ESIPT-active regenerable fluoro-chromogenic molecular tweezers **NPDM** was employed for the fast detection of Al^{3+} ions.